

pubs.acs.org/cm Article

Deciphering Defects in Yb_{2-x}Eu_xCdSb₂ and Their Impact on Thermoelectric Properties

Ashlee K. Hauble, Caitlin M. Crawford, Jesse M. Adamczyk, Maxwell Wood, James C. Fettinger, Eric S. Toberer, and Susan M. Kauzlarich*



Cite This: Chem. Mater. 2022, 34, 9228-9239



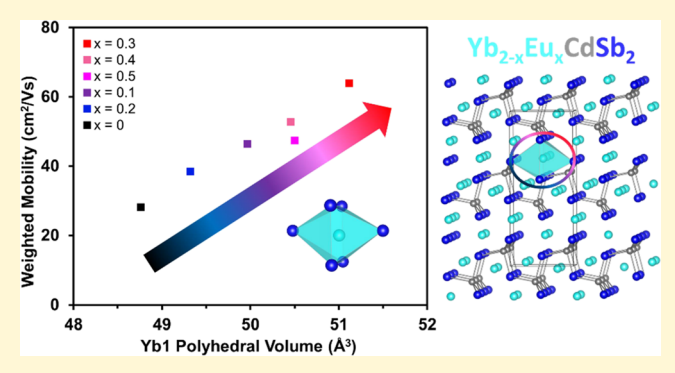
ACCESS I

III Metrics & More

Article Recommendations

s Supporting Information

ABSTRACT: Layered Zintl phases with A_2MPn_2 stoichiometry are an underexplored class of potential thermoelectric materials with complex and diverse chemistry. The solid solution $Yb_{2-x}Eu_xCdSb_2$ is an example of the promise these compounds hold, as one composition, $Yb_{1.64}Eu_{0.36}CdSb_2$, has reported one of the highest zTs of any Zintl phase material at 525 K. The present study examines changes in structure and bonding of this solid solution that impacts thermoelectric performance. Pair distribution function analysis is combined with electronic structure modeling to take a chemical bonding-based approach to deconvolute the impact of defects on thermal and electronic properties in $Yb_{2-x}Eu_xCdSb_2$. $Yb_{2-x}Eu_xCdSb_2$ (x=0, 0.1, 0.2, 0.3, 0.4, 0.5) samples were synthesized, and thermoelectric properties and defect



chemistry were investigated. Samples from the middle of the series x = 0.2 and 0.3 were found to be the most highly defected, exhibiting Yb and Sb vacancies, as well as distortions in the Yb-Sb coordination spheres that correlate with thermoelectric properties. The highest efficiency is reported for x = 0.4 ($zT \approx 0.9$ at 525 K), and the thermoelectric quality factor predicts that x = 0.3 could achieve zT > 2 by synthetically tuning the defect structure and thereby carrier concentration. The strategy of investigating local structure outlined in this study can be applied to a variety of other thermoelectric materials to provide insight into the hidden role of defect chemistry in understanding the structure-property relationships in extended solids.

1. INTRODUCTION

The world's rising demand for energy is driving research for renewable electricity solutions, as well as ways to make current technologies more efficient. Thermoelectric generators (TEGs) are one option that could help slow climate change by providing a power source that is not dependent on the combustion of fossil fuels. TEGs convert waste heat directly to electricity via the Seebeck effect, where charge carriers are driven from the hot side of a thermal gradient to the cold side to relieve thermal energy. This is an important technology, given that only about one-third of the energy currently consumed in the world is effectively used, with most being lost as heat. One area where TEGs could shine is industrial waste heat scavenging. If harnessed, waste heat from industrial processes in the United States could provide more than 10 gigawatts of electricity, enough to power 10 million homes and save industries more than \$3 billion a year.² TEGs could also be used to generate electricity from natural heat sources, such as the sun.³ For these applications and many others, discovery and optimization of thermoelectric materials that exhibit high heat to electricity conversion efficiency in the 100-500 °C range is an active area of research.²

The conversion efficiency of a thermoelectric material is defined by the unitless figure of merit, $zT = (S^2T)/\kappa\rho$ where S is the Seebeck coefficient, T is the operating temperature, κ is the thermal conductivity, and ρ is the electrical resistivity. The primary challenge in designing thermoelectric materials is decoupling these interrelated properties, a task that layered Zintl phase semiconductors are well suited for given that their structures include both ionic and covalent bonding.3- A_2MPn_2 (A = alkaline earth, Yb, Eu; M = transition metal, Pn = group 14 element) Zintl phases in particular comprise a promising and underexplored family of potential thermoelectric materials. More than 20 compounds and three major structure types have been discovered, most of which are narrow band gap semiconductors.4 Several A2MPn2 compounds have also been predicted to be good p-type thermoelectric materials at low temperatures.^{4,7}

Received: August 5, 2022 Revised: September 17, 2022 Published: October 6, 2022





thermoelectric properties have only been reported for a handful of compounds, leaving plenty of room for further investigation. The most promising compounds that have been measured, $\mathrm{Eu_2ZnSb_2}^{8-10}$ and $\mathrm{Yb_{2-x}Eu_xCdSb_2}^{11}$ exhibit zTs comparable to $\mathrm{YbZn_2Sb_2}^{12}$ $\mathrm{Zn_4Sb_3}^{13-15}$ and $\mathrm{TAGS^{16}}$ at temperatures relevant for energy applications on earth and serve as indications of the great thermoelectric potential that could be uncovered in this class of layered Zintl phases. $^{1,2,9-12,16}$ While $\mathrm{Eu_2ZnSb_2}$ and $\mathrm{Yb_{2-x}Eu_xCdSb_2}$ are both layered structures with similar composition, their structures differ, with $[\mathrm{ZnSb_2}]^{4-}$ having a defect honeycomb structure and $[\mathrm{CdSb_2}]^{4-}$ having an undulating layered structure.

This diverse bonding, if well understood, gives researchers a great deal of control in tuning properties. In a simple picture, the covalent networks in these layered structures are largely responsible for electrical transport¹⁷ and the interspersed cations create disorder that helps scatter phonons and reduce thermal conductivity. However, in some structure types, cations play a key role in controlling carriers, and the chemistry of each compound must be investigated carefully to enable optimization of zT. Compounds with AM₂Pn₂ and A₂MPn₂ stoichiometry illustrate an example of the benefits and drawbacks of this generalized understanding of layered structures.¹⁷ Recent studies have emphasized the importance of cation bonding, identity, disorder, and defects in $Yb_{2-x}Ca_xCdSb_2$, $Ca_{2-x}Eu_xCdSb_2$, $Yb_{2-x}Eu_xCdSb_2$, $Ca_{2-x}Lu_xCdSb_2$, A_2CdP_2 (A = Ba, Sr), and AZn_2Sb_2 (A = Ca, Sr, Yb, Eu) in determining electronic properties and structure type. $^{12,18-23}$ In addition, studies on Mg₃Sb₂ have revealed that the Zintl formalism does not adequately describe interactions between cations and [Mg₂Sb₂]²⁻ slabs in AMg₂Pn₂ compounds, which cannot be considered layered structures due to isotropic bonding networks, even though they adopt the CaAl₂Si₂ structure type. ^{24,25} These examples highlight the need for better understanding of chemical bonding, defects, and local structure in each system to enable optimization of thermoelectric properties.

In some materials, cation substitution can also be used to tune defect structure and vary carrier concentration while simultaneously reducing lattice thermal conductivity. 21,26-28 In materials where the valence band edge is sensitive to cation identity, such as $Yb_{2-x}Eu_xCdSb_2$ and $Ba_{2-x}Sr_xCdP_2$, solid solutions are useful tools for band engineering. 18,19,22 This is especially true when paired with electronic structure calculations that show which molecular orbitals are located near the Fermi level. Using density of states (DOS) calculations as a guide, chemical intuition can be applied to tune the relevant orbital interactions and improve properties while gaining a deeper understanding of the structure. Crystal orbital Hamilton population (COHP) curves can also be used to assist in understanding the influence of defects and disorder on bonding when paired with a local structure analysis technique such as pair distribution function (PDF) analysis.

This investigation was motivated by the exciting properties reported for one composition in the $Yb_{2-x}Eu_xCdSb_2$ system, x = 0.36, and the possibility that compositions on either side of x = 0.36 might show even better thermoelectric properties. Given recent studies that have highlighted the sensitivity of this material to cation substitution, showing that subtle shifts in bonding drive a transition to a different structure type, obtaining a more complete picture of how the structure changes with cation substitution is critical. ^{18,19,29} Additionally,

understanding the chemical origins of these excellent properties provide an improved framework for designing more efficient thermoelectric materials with this structure type. The analyses of the impact of local defect structure on chemical bonding and electronic transport also provide a framework for understanding defects from a structure-property perspective that can be broadly applied to Zintl phases. The present work offers an examination of the $Yb_{2-x}Eu_xCdSb_2$ composition (x = 0, 0.1, 0.2, 0.3, 0.4, and 0.5) to provide insight to the thermoelectric properties. An improved synthetic method employing EuH2 as a reactive precursor to facilitate mixing is presented. This reagent eliminated a Yb_{11-x}Eu_xSb₁₀ impurity that was present when elemental Eu was used as a precursor. The structure is investigated with single crystal and powder Xray diffraction with PDF analyses and thermoelectric properties from 323 to 523 K measured.

2. EXPERIMENTAL SECTION

2.1. Synthesis. Single crystals of Yb_{2-x}Eu_xCdSb₂ were synthesized according to the literature procedure. The elements (Yb (Edge Tech, 99.95%), Eu (Stanford Materials, 99.99%), Cd (shot, Alfa Aesar, 99.95%), and Sb (shot, 5NPlus, 99.999%)) were combined in a 2-x:x:1:2 molar ratio along with 10 molar equivalents of Pb flux (Pb needles, Alfa Aesar, 99.99%) in a 5 mL alumina crucible set for a total mass of \sim 3 g. Samples were made for Eu concentrations of x = 0, 0.1, 0. 2, 0.3, 0.4. The crucibles were sealed into silica tubes evacuated to <50 mTorr, placed upright in a box furnace, and heated at 120 °C/h to 960 °C where they dwelled for 20 h and were cooled to 500 °C at 5 °C/h. The flux was removed by hot centrifugation, and the tube was opened in an argon-filled glove box, where crystals were selected for X-ray diffraction.

Polycrystalline Yb2-xEuxCdSb2 samples were synthesized as follows: in an Ar-filled glove box, Sb shot was loaded into a 5 mL tungsten carbide ball mill with two 8 mm tungsten carbide balls and sealed with tungsten carbide end caps fitted with Viton O-rings. The canister was hermetically sealed in two Uline 4 mil polyethylene bags, milled in an SPEX 8000 M mixer mill for 15 min, and then transferred to a glove box. After scraping with a metal spatula, Yb filings, EuH₂ (American Elements), and cut Cd pieces in a stoichiometric ratio of 2-x:x:1 were added to the Sb powder for a total reaction mass of ~ 3 g. All four substituents were milled together for 30 more min, and the container was again transferred to the glove box to be scraped before milling for an additional 20 min to ensure that the elements were intimately mixed before the resulting powder was loaded into a Nb tube. The Nb tube was sealed in an Ar-filled arc welder and placed inside a fused silica tube, evacuated to <50 mTorr, and sealed. The jacketed Nb tube was put into a box furnace to be annealed. For Eucontaining Yb_{2-x}Eu_xCdSb₂ samples, the temperature was increased at a rate of 120 °C/h to 800 °C and annealed at that temperature for 96 h. Phase pure Yb₂CdSb₂ was not able to be synthesized at the same temperature, and the heating profile had to be adjusted to anneal at

All thermoelectric and PDF data were collected on the same set of polycrystalline samples. Three independent batches of samples were made and measured to confirm reproducible results.

- **2.2. Spark Plasma Sintering.** The annealed black powder was then ground, sieved (100 mesh), and loaded into a graphite die with a diameter of 12.7 mm which was hermetically sealed with graphite foils. The powder was consolidated using a Dr. Sinter Junior Spark Plasma Sintering system (Fuji Electronic Indus-trial Co., LTD) under ~385 torr of Ar. The sample was heated to 550 °C, where it was left to dwell for 15 min. The force was slowly increased from 6 to 10.5 kN, beginning at 350 °C. The geometric densities of the resulting pellets were determined to be >95% of the theoretical value.
- **2.3. Single Crystal X-ray Diffraction.** Silver needle-like crystals were selected in Paratone oil in air and mounted on the goniometer of a Bruker APEX DUO CCD X-ray diffractometer with Mo K α radiation (λ = 0.71073 Å) at 90 K with a crystal detector distance of 5

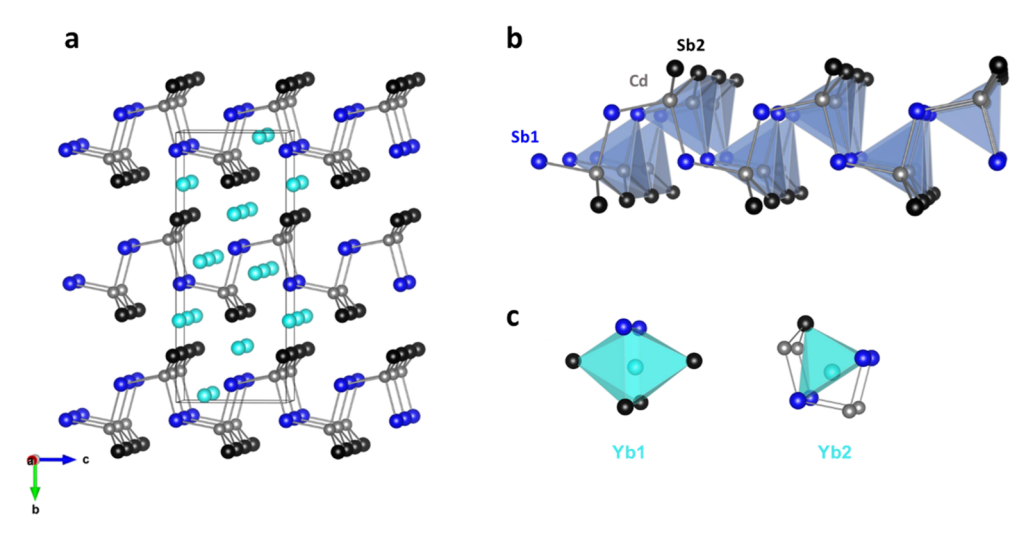


Figure 1. (a) Crystal structure of $Yb_{2-x}Eu_xCdSb_2$. Turquoise spheres represent Yb/Eu, gray spheres represent Cd, dark blue spheres represent Sb1, and black spheres represent Sb2; (b) anionic corner-shared $[CdSb_{4/2}]^{4-}$ tetrahedral chains. Sb1 sites shown in blue and Sb2 shown in black; (c) Yb1 interlayer and Yb2 intralayer coordination environments.

cm. The unit cell was indexed using three sets of 0.5° wide ω -scans, 10 s per frame, and 30 frames per set. Additional data collection included four ω -scan data frame series with 0.3° wide scans, 20 s per frame and 606 frames per series with at 32.0° , and with $\varphi = 0^{\circ}$, 90° , 180° , and 270° . The program SAINT was used to correct for Lorentz and polarization effects, and SADABS was utilized to correct for absorption and merge the data. SHELXTL software was used to determine a space group. ¹⁵ The structure was then determined using XT and further refined with XL. All structure solutions (CSD 2194398-2194400) agreed well with those previously described. ^{9,13,16}

- **2.4. Powder X-ray Diffraction.** Polycrystalline sample purity was assessed using powder X-ray diffraction. Pellets of the polycrystalline samples were cut with a diamond saw, and a piece was ground into a fine powder with an agate mortar. Data were collected using a Bruker D8 Advance diffractometer with Cu K α radiation operated at 40 kV and 25 mA at room temperature with 2θ range 20-75° with a 0.015° interval and a scan rate of 1 s per step. $Yb_{2-x}Eu_xCdSb_2$ was confirmed to be the majority phase via Rietveld refinement, which was carried out using TOPASS software.³²
- **2.5. Pair Distribution Function (PDF) Analysis.** Total scattering data on all polycrystalline pressed pellets were collected at beamline 11-ID-B at the Advanced Photon Source via the mail-in program. The sintered, polycrystalline samples were ground with a mortar and pestle and loaded into 0.8 mm inner diameter Kapton capillary tubes prior to data collection. X-ray wavelength was 0.2115 Å, and intensities were measured with a 2D area detector with a distance of 180 mm with maximum wave vector $q = 24 \text{ Å}^{-1}$. The 2D images were integrated using GSAS-II and converted to G(r) using pdfgetx3. Refinements were carried out using the small box method in PDFgui starting with a crystallographic information file (CIF). 33,34
- **2.6. Elemental Analysis and SEM Imaging.** Pelletized, polycrystalline samples were mounted in epoxy discs and polished using sandpaper and a polishing wheel (1 μ m colloidal diamond suspension) prior to analysis. Stoichiometry was determined via energy-dispersive spectroscopy (EDS) using an FEI Scios DualBeam FIB/SEM with an Oxford Instruments X-Max50 50 mm² Si drift detector and 15 kV accelerating voltage. An Everhart—Thornley detector was used to collect secondary electron images with 20 kV accelerating voltage.
- **2.7. Thermoelectric Properties.** Thermal diffusivity was measured on the sintered, polycrystalline pellets using a Netzsch laser flash analysis instrument, and thermal conductivity was calculated from diffusivity using the equation $\kappa = \lambda \rho C p$, where κ is the thermal conductivity, C p is the heat capacity (calculated using the Dulong–Petit equation, which was reported to be consistent with

measured heat capacity), 11 λ is the diffusivity, and ρ is the sample density.

High-temperature measurement of the Seebeck coefficient was performed from 323 to 523 K in steps of 10 K using a custom-built apparatus previously described.³⁵ An atmosphere of low pressure nitrogen (5 torr) was used during the Seebeck measurements to ensure good thermal contact between the sample, heater blocks, and measurement thermocouples. Graphite foil spacers placed between the measurement thermocouples and the sample protect the thermocouple junction from contamination and ensure high quality measurements. All samples underwent a minimum of 2 heating and cooling cycles during measurement to ensure that samples were not undergoing evolution during measurement. High-temperature resistivity and Hall effect measurements were performed on a custom-built apparatus with a Van der Pauw geometry from 323 to 523 K under vacuum. 36,37 Test current values of 0.1 A and a magnetic field value of 1 T were used for the measurements. Confirmation of ohmic contacts was determined before each measurement by generating a currentvoltage curve across all combinations of contacts.

3. RESULTS AND DISCUSSION

3.1. Structure and Composition. Figure 1a illustrates the crystal structure of Yb_{2-x}Eu_xCdSb₂ (orthorhombic space group Cmc2₁), as determined by single crystal X-ray diffraction. It is a layered Zintl phase composed of anionic corner-shared [CdSb_{4/2}]⁴⁻ tetrahedra connected to form an undulating layered structure that are separated by layers of Yb²⁺ and Eu²⁺ cations. The two unique Sb sites are shown in Figure 1b. Sb1 (blue) links the chains in the *c*-direction, while Sb2 (black) connects the layers in the a-direction. There are two unique cation sites, and the polyhedra are highlighted in Figure 1c: a Yb1 interlayer site and a Yb2 intralayer site. Eu preferentially occupies the larger interlayer Yb1 site (Figure 2), consistent with previous reports. 11,18,19,38 In the case of the highest Eu concentration of the crystals investigated herein, x = 0.42, the preference is for the interlayer site (Yb1), although there is a small amount on the intralayer Yb2 site. Table 1 outlines relevant single crystal data, including lattice parameters, which increase with increasing Eu concentration, as expected due to the larger ionic radius of Eu compared to Yb.

Here, we focused on synthesizing a series of x values close to the best thermoelectric composition reported: x = 0.36. We employed EuH₂, a salt-like precursor that aids in mixing the

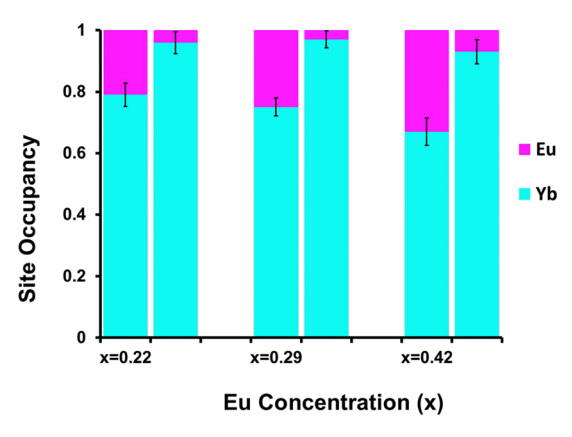


Figure 2. Occupancy of the Yb1 and Yb2 sites in $Yb_{2-x}Eu_xCdSb_2$ by Eu and Yb for single crystals of varying Eu contents. Eu preferentially occupies the larger, interlayer octahedral site.

elements and provides a clean byproduct of hydrogen gas during the reaction. The polycrystalline samples are from milled powders of the constitutional elements that were annealed in silica jacketed niobium tubes prior to spark plasma sintering densification into pellets. Stoichiometry of polycrystalline pellets was confirmed by EDS (Table 2 and Figure S1), and elemental maps are given in Figure 3a. Eu content was in good agreement with the preparative amount, and the elemental maps show that it was dispersed evenly throughout the sample, highlighting the advantage of using a EuH₂ precursor.

Because of the good agreement between nominal and experimental compositions, nominal compositions will be employed to describe the samples. Secondary electron micrographs (Figure 3b) confirm the high density of the pellets (<95% of theoretical value), and backscattered electron micrographs confirm homogeneity via Z contrast imaging (Figure 3c).

Figure 4 shows the powder X-ray diffraction (PXRD) patterns for polycrystalline Yb_{2-x}Eu_xCdSb₂ pressed pellet samples. All samples show a small impurity (<4% by weight for all samples) that is attributed to YbCd₂Sb₂. Because the amount is small and consistent throughout the series, the thermoelectric measurements provided here should be

Table 2. Eu Content Determined by EDS for Polycrystalline Pelletized Samples

preparative Eu content (x)	experimental Eu content (x)
0	0.00
0.1	0.11(6)
0.2	0.17(1)
0.3	0.27(3)
0.4	0.35(1)
0.5	0.51(2)

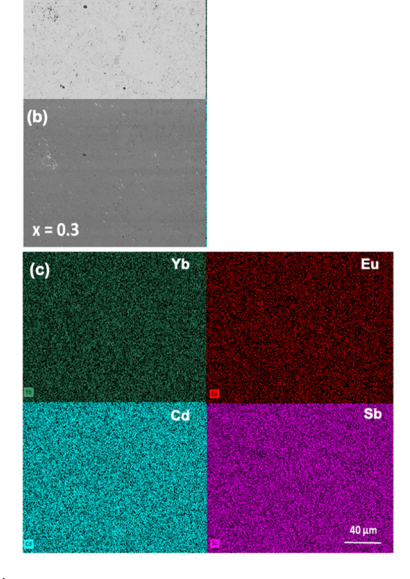


Figure 3. (a) Backscattered electron image of $Yb_{1.7}Eu_{0.3}CdSb_2$ shows Z contrast and homogeneity. (b) Secondary electron image shows topography; (c) elemental maps from EDS are shown for Yb, Eu, Cd, and Sb. Images confirm that elements are well dispersed and the sample is homogeneous.

representative of the systematic change in the properties of the majority phase, $Yb_{2-x}Eu_xCdSb_2$. The observed diffraction peaks shift left with increasing Eu concentration, indicating that the unit cell volume increases, consistent with single crystal data and Figure 5. The b lattice parameter, which is in

Table 1. Data Collection Details and Selected Single Crystal Parameters for Yb_{2-x}Eu_xCdSb₂ (x = 0.22, 0.29, 0.42)

empirical formula	$\mathrm{Yb}_{1.78(2)}\mathrm{Eu}_{0.22}\mathrm{CdSb}_{2}$	$\mathrm{Yb}_{1.71(3)}\mathrm{Eu}_{0.29}\mathrm{CdSb}_{2}$	$\mathrm{Yb}_{1.58(3)}\mathrm{Eu}_{0.42}\mathrm{CdSb}_{2}$
crystal system	orthorhombic		
space group, Z	Cmc2 ₁ (no. 36), 4		
T (K)	90 K		
a (Å)	4.6317(7)	4.6367(13)	4.6393(15)
b (Å)	17.518(3)	17.566(5)	17.607(6)
c (Å)	7.1942(11)	7.204(2)	7.205(2)
volume (ų)	583.71(15)	586.8(3)	588.5(3)
density (calculated, g/cm ³)	7.94	7.88	7.82
absorption coefficient (cm ⁻¹)	43.1	42.5	41.7
reflections collected	3386	3779	4624
independent reflections	990	758	1005
flack parameter	0.403	0.379	0.040
R_1 , wR_2 $(I > 2\sigma(I))$	0.0181, 0.0381	0.0129, 0.0316	0.0177, 0.0400
goodness of fit	1.11	1.239	1.064
largest diff. peak/hole (e ⁻ /Å ³)	1.142/-1.324	1.253/-1.762	1.544/-2.342
deposited CIFs (CSD) reference numbers	2194398	219399	2194400

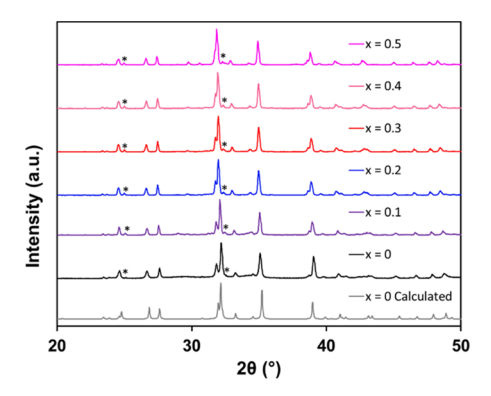


Figure 4. PXRD patterns post SPS of $Yb_{2-x}Eu_xCdSb_2x = 0$, 0.1, 0.2, 0.3, 0.5 samples compared with the calculated diffraction pattern for x = 0. The asterisk marks the largest diffraction peak for the $YbCd_2Sb_2$ impurity.

the stacking direction of the layers, exhibits the greatest increase with Eu concentration and is consistent with Eu preferentially occupying the interlayer site. The c lattice parameter from PXRD data is notably larger than those observed for the single crystal samples. This suggests a distortion of the tetrahedrally coordinated $[CdSb_{4/2}]^{4-}$ that extends along the c axis. The large c axis is likely due to structural disorder, which was investigated using PDF analysis. 3.1.1. Pair Distribution Function (PDF) Analysis. PDF

3.1.1. Pair Distribution Function (PDF) Analysis. PDF analysis was employed to identify local deviations from the nominal structure and short-range structural disorder. Refinement of short r-range (2.5–5 Å) atomic site occupancies revealed significant cation deficiencies on the interlayer Yb1 site for x = 0.2-0.5, while the intralayer Yb2 site was fully occupied with the mixed cations Yb/Eu for all samples. Figure 6a shows that x = 0.3 has the lowest Yb1 occupancy. The variation in cation occupancies could be due to changing

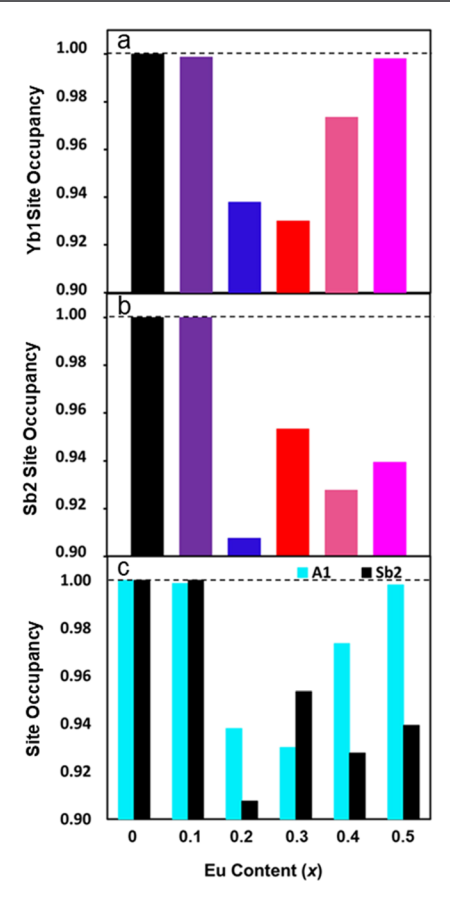


Figure 6. Site occupancy as determined by short *r*-range PDF analysis for different Eu concentrations for (a) Yb1 cation site and (b) Sb2 site; (c) comparison of the Yb1 site occupancy and Sb2 site occupancy. The cation site is in turquoise, and the Sb site is in black. The dotted lines mark a site occupancy of 1 for reference.

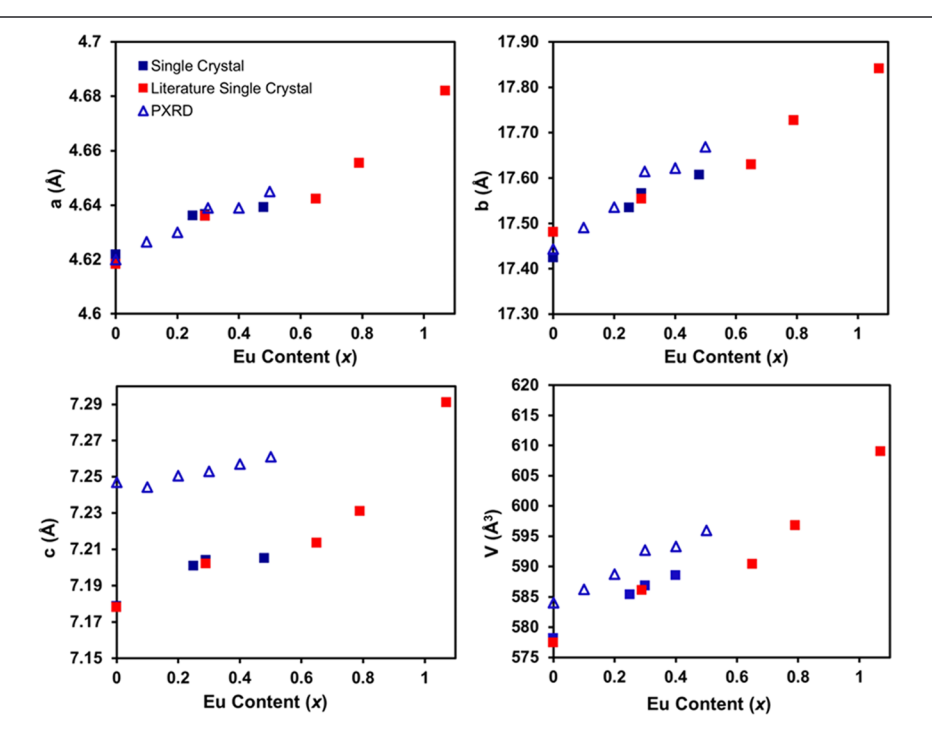


Figure 5. Lattice parameters from single crystal (this work (90 K) and literature ref 30, (170 K)), and PXRD (room temperature) are plotted as a function of Eu content. Lattice parameters increase with increasing Eu content.

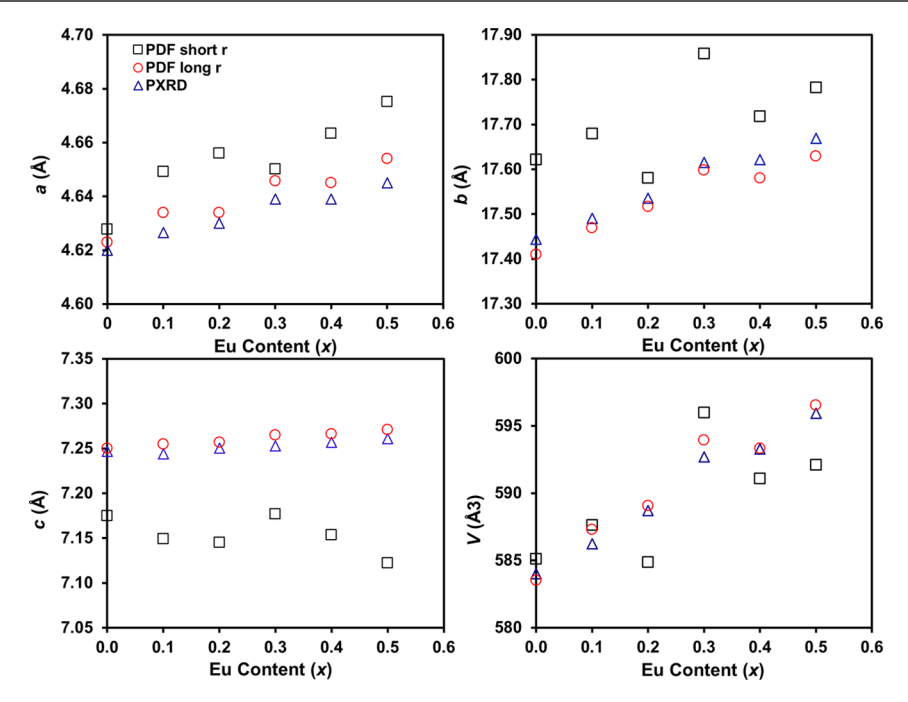


Figure 7. Lattice parameters from Rietveld refinement (blue triangles), PDF from 2.5 to 5 Å (black squares), and PDF from 2.5 to 20 Å (red circles).

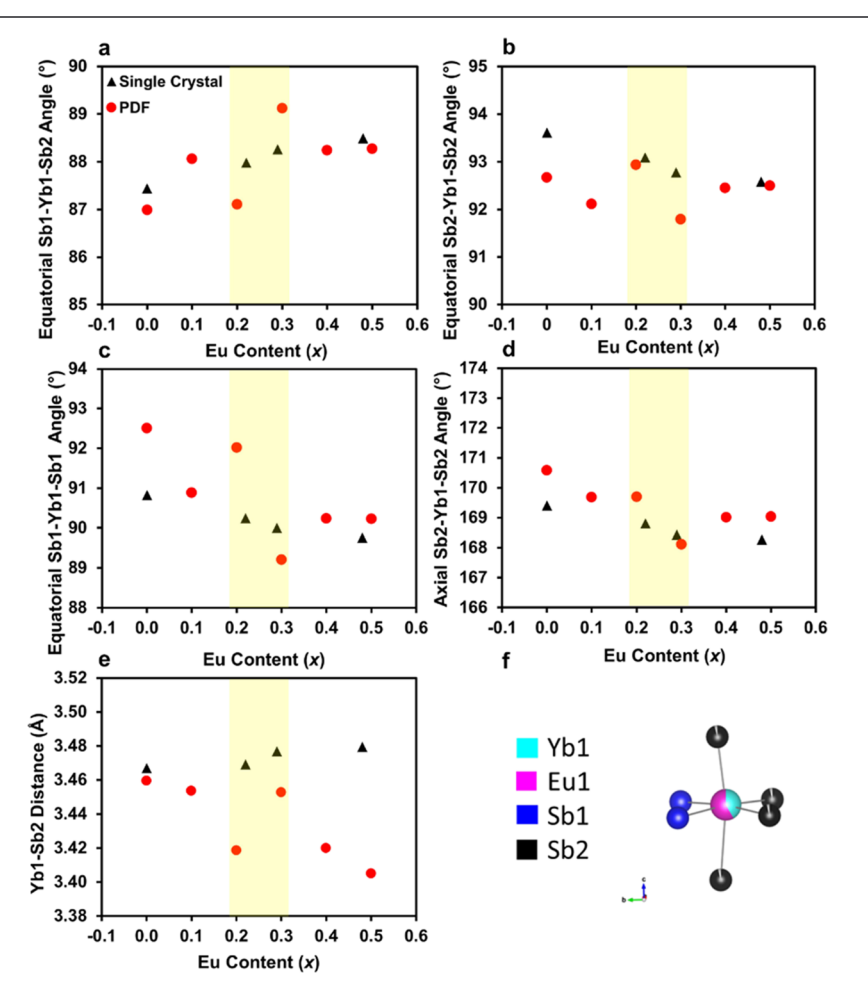


Figure 8. Bond angles for Yb1 octahedra determined by single crystal XRD (black triangles) performed on single crystal samples and short-range PDF analysis (red circles) performed on polycrystalline samples. (a) Equatorial Sb2-Yb1-Sb2 bond angle; (b) axial Sb2-Yb1-Sb2 bond angle; (c) Sb1-Yb1-Sb1 bond angle; (d) Sb1-Yb1-Sb2 bond angle; (e) Yb1-Sb2 bond distance; (f) Yb1 octahedron from x = 0.5 for reference. The yellow highlights the compositions x = 0.2 and 0.3, which deviate from the trend.

defect energy with Eu, as seen in related Zintl phase AZn_2Sb_2 (A = Yb, Eu, Sr, Ca). In the AZn_2Sb_2 system, cation vacancies are the dominant native defect, and equilibrium defect concentration has been shown to vary with the electronegativity of the cation.²¹

Based on this reasoning, cation vacancies are expected to be the primary donor defect in this p-type semiconductor. However, the number of vacancies does not trend systematically with Eu amount, suggesting that factors other than cation substitution control defect energies. With these cation defects, Figure 6b shows that there are also Sb defects. Similar to the two cation sites, deficiencies were only present on the Sb2 sites and all Sb1 sites were fully occupied. Sb vacancies are expected to be "killer" acceptor defects that limit the number of free carriers that can be introduced through cation vacancies, similar to the Ca_{11-x}RE_xSb_{10-y} system, which can contain up to 20% Sb deficiencies to prevent population of antibonding orbitals and stabilize the structure.³⁹ Defect diagrams calculated for Ca₅Al₂Sb₆ and A₂CdP₂ (A = Sr, Ba, with the same structure type as Yb₂CdSb₂) have also shown that pnictide vacancies are expected to be the lowest energy defects in these Zintl phases. 40,41 COHP curves calculated by Kim et al. for the related compound, Yb_{1.5}Ca_{0.5}CdSb₂, which is in this structure type reveal A1-A1 bonding states (A1 as a more generalized notation for the Yb/Eu/Ca1 mixed site) 0-0.25 eV below the E_F and Cd-Sb antibonding states from ~0.25 to 0.5 eV below $E_{\rm F}$. The Cd-Sb antibonding states may limit the p-type dopability window, resulting in charge compensating Sb defects to stabilize the compound by filling the bonding A1-A1 states. Figure 6c compares Yb1 and Sb2 site occupancies and shows that the largest amounts of site defects are for compositions x = 0.2, 0.3. Interestingly, x = 0.2, 0.3 are the most cation deficient (Yb1 site occupancies 0.94 and 0.93, respectively), but their Sb content varies. For these compositions, x = 0.2 is more Sb deficient, whereas x = 0.3is more cation deficient. The lack of a systematic trend here could be explained by changes in the Yb1-Yb1 site bonding as different amounts of Eu are incorporated that alter the dopability window, possibly including additional Eu-Sb interactions as seen in the coinage-metal-stuffed Zintl phase Eu_oCd₄Sb₉. 11,42 The variation in cation and Sb content between samples is expected to affect electronic properties.

Short r-range PDF analysis indicates that the local structure differs from the average structure, observable from differences in lattice parameters (Figure 7). Lattice parameters determined by PDF from r-range 2.5 to 5 Å deviate from those determined by Rietveld refinement of PXRD data and long r-range PDF for all compositions. The a and b axes are larger than the average structure, while the c axis is smaller, indicating stretching of the stacking axis and compression of the $[CdSb_{4/2}]^{4-}$ chains. Additionally, lattice parameters for x=0.2 and 0.3 deviate substantially from the expected trend with x=0.2 having the smallest unit cell volume, while x=0.3 has the largest. Close examination of bond lengths and angles from PDF analysis and single crystal data shows that distortions in Yb1–Sb octahedra are responsible for the variation in lattice parameters.

Analysis of single crystal refinements shows linear changes in all four bond angles in Yb1–Sb octahedra as Eu substitutes (Figure 8). The Sb1–Yb1–Sb2 bond angle increases to make room for the neighboring Eu atom, which is larger than Yb, in the *a*-direction. Equatorial Sb2–Yb1–Sb2 and Sb1–Yb1–Sb1 angles decreased with Eu substitution, which can be explained by steric and electronic effects of replacing the smaller, more

electronegative central Yb atom with larger, less electronegative Eu. Bond angles obtained from PDF analysis of polycrystalline samples do not show the same linear trend, which indicates that the local structure deviates from the average structure given by the single crystal refinement. These distortions may be a result of the large number of cation and Sb defects. Given the differences between local and average structure, predictions based on single crystal structures may not fully explain experimental properties observed in sintered polycrystalline samples as vacancy ordering can alter band structure, as shown in Eu₂ZnSb₂. §

The most notable differences between single crystal and PDF bond angles are for x = 0.2 and 0.3. While x = 0.2 exhibits unexpectedly large equatorial Sb2-Yb1-Sb2 and Sb1-Yb1-Sb1 bond angles, x = 0.3 exhibits unexpectedly small angles for the same bonds. This results in a small equatorial Sb1-Yb1-Sb2 angle for x = 0.2 and small Sb1-Yb1-Sb1 for x = 0.3. In addition, the axial Yb1-Sb2 bond length is shorter than expected for x = 0.2 and longer for x = 0.3 (Figure 8e). The fluctuations in these angles and lengths result in distortions in the coordination environment of Yb1 for x = 0.2 and 0.3, as well as elongation of the a axis and compression of the a axis for a axis with elongation of the a axis for a axis for

The observed distortions in the Yb1 coordination environment can be understood by considering the electronics of Sb2–Cd bonding and Yb1–Yb1 bonding. An electron localization function analysis done on Yb_{2-x}Ca_xCdSb₂ in this structure type showed greater distribution of lone pairs on the Sb2 site compared to Sb1, which leads to a smaller Cd–Sb2–Sb angle due to the repulsive interaction of the excess electron density and the Cd–Sb2 bonding pairs. ¹⁹ The large number of vacancies on the Sb2 site in x = 0.2 allows the Cd–Sb2–Cd bond angle to relax (Figure 9a), distorting the *a*-direction of the covalent chains. This opening of the Cd–Sb2–Cd bond angle results in a larger equatorial Sb2–Yb1–Sb2 angle and

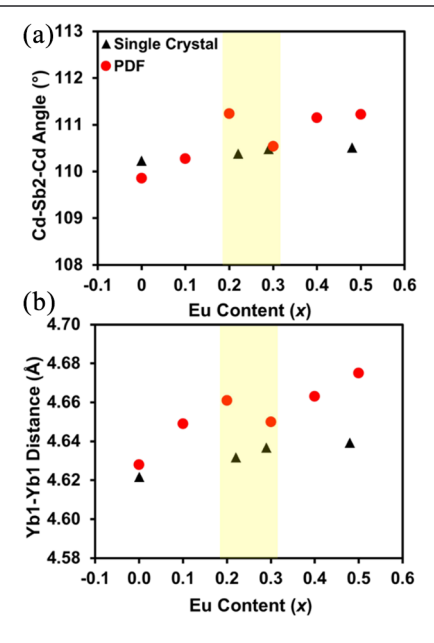


Figure 9. (a) Cd–Sb2–Cd and (b) Yb1–Yb1 angles from single crystal XRD (black triangles) and short-range PDF analysis (red circles) of polycrystalline samples. The yellow box highlights compositions x = 0.2 and 0.3, which deviate from the trend.

thus a smaller Sb1–Yb1–Sb2 angle. Integrated COHP curves of Yb₂CdSb₂ and Ca₂CdSb₂, polytypes with identical layers but differing stacking sequences that lead to crystallization in *Cmc*2₁ and *Pnma* space groups, respectively, indicated that stronger (Yb/Ca)1–Sb bonding in the *Cmc*2₁ structure plays a key role in directing the structure transition of the solid solution. This finding suggests that the Yb1–Sb coordination sphere is an important factor for the stability and electronic properties of Yb₂CdSb₂.

Yb1-Yb1 distances, plotted in Figure 9b, are also of interest in this compound. For short-range PDF analysis, atomic distances in the a-direction show two distinct trends: increasing linearly from x = 0 to x = 0.2 before dropping at x = 0.3 and then increasing linearly to x = 0.5. Single crystal bond distances increase systematically as Eu is added. The variation in atomic distances could be explained by optimized Yb1—Yb1 bonding for each Eu composition given the distorted coordination environments in polycrystalline samples. In another theoretical study of the two polytypes of A2CdSb2 (A = Ca, Yb) by Kim et al., electronic interactions were analyzed for both structure types in order to determine the important driving forces leading to increased stability in one structure type over the other. 19 Their calculations showed that the crystal structure is sensitive enough to A1-A1 bonding interactions that optimization of A1-A1 distances drives the transition from the related Ca₂CdSb₂-type Pnma structure to the Yb₂CdSb₂-type Cmc2₁ structure as more Yb is incorporated. The Pnma structure of Ca₂CdSb₂ has two unique A1-A1 bond distances, one long and one short, while the Cmc2₁ structure of Yb₂CdSb₂ has only one distance with an intermediate length that alleviates a repulsive A1-A1 interaction from the shorter bond in the Pnma structure for Yb-rich compositions, replacing an antibonding A1-A1 interaction with a slightly bonding one just below the Fermi level. The more energetically favorable A1-A1 bonding stabilizes Yb2CdSb2 in the Cmc21 space group. Given the sensitivity of this system to the A1-Sb and A1-A1 interactions discussed above, such distortions in Yb1 octahedra would be expected to impact the electronic properties. 18,19

3.2. Electronic Properties. Seebeck coefficients (S) and electrical resistivity (ρ) values (Figure 10a,b) do not trend systematically with Eu, suggesting that factors beyond cation substitution play an important role in the electronic structure of this compound. Notably, x=0.3 has the smallest Seebeck coefficient and lowest resistivity, while x=0.2 has the largest Seebeck coefficient and highest resistivity. This can be explained by examining changes in weighted mobility (μ_w) with distortions in the Yb1 octahedra discussed above. μ_w is defined as charge carrier mobility weighted by the density of

electron states according to the relationship $\mu_{_{
m W}} pprox \mu \Big(rac{m^*}{m_{_{
m c}}} \Big)^{3/2}$

(where μ is the mobility, m^* is the effective mass, and $m_{\rm e}$ is the electron mass) and is a carrier concentration independent indicator of the inherent quality of electronic transport properties of a material. When a single isotropic parabolic band dominates charge transport, $\mu_{\rm w}$ is constant at a given temperature, regardless of the doping level. This makes it a useful way to detect changes in band structure due to alloying—if changes in electronic properties are due to carrier concentration alone, $\mu_{\rm w}$ will have the same value for all samples in a series. At 525 K, $\mu_{\rm w}$ in this system increases with Yb1 polyhedral volume (Figure 10c), indicating that the band structure changes as the Yb1–Sb octahedron is distorted. This

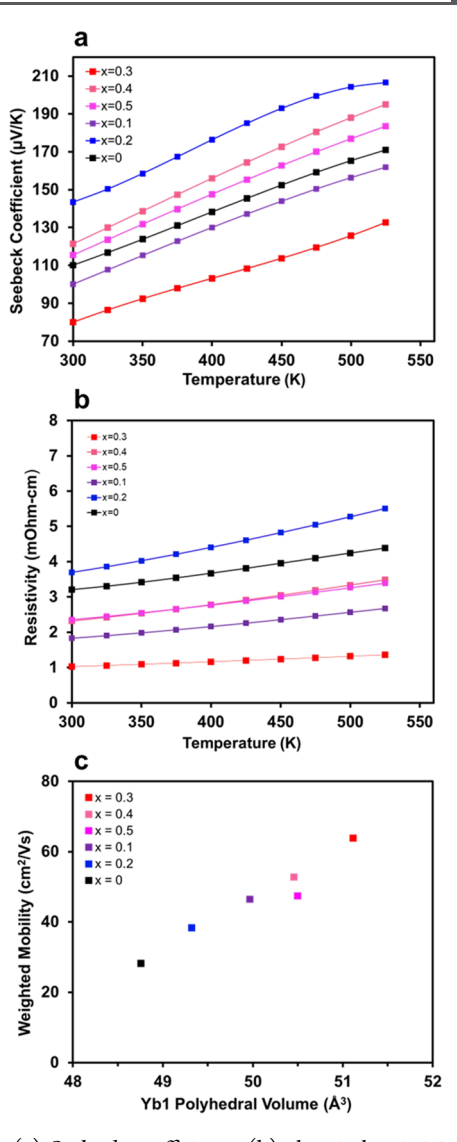


Figure 10. (a) Seebeck coefficients, (b) electrical resistivity, and (c) weighted mobility for $Yb_{2-x}Eu_xCdSb_2$ at 525 K. Points are color-coded in a gradient according to weighted mobility.

agrees well with previous studies discussed above that have shown this structure to be highly sensitive to Yb1 bonding and small changes in interatomic distances dramatically affect bonding and antibonding states just below the Fermi level. ^{18,19} The published projected DOS suggests that the valence band is composed of Yb/Eu 5d, Sb 5p, and Cd 5p states, ¹¹ so changes in Yb1–Yb1, Y1b–Sb, and Cd–Sb bonding are likely to affect the electronic structure of the valence band.

Weighted mobility, $\mu_{\rm w}$, is the lowest for the parent compound, which shows that Eu incorporation improves the intrinsic thermoelectric quality of the material. The next lowest $\mu_{\rm w}$ is observed for x=0.2, which has the smallest Yb1 octahedral volume of all Eu-containing samples. The shorter bond lengths indicate better orbital overlap and stronger interactions, which leads to broader band dispersion, lower DOS, and a smaller effective mass of charge carriers. Weighted mobility is weighted by the effective mass of charge carriers in a sample, so it is not surprising that the polyhedral volume and weighted mobility are related. However, this change in bonding could be impacting transport in the materials studied here in several different ways. For example, distortions in the

Yb1 coordination sphere that lead to less dispersion in the valence band maximum could lead to these deeper bands moving up in energy to create a convergence type event, which would improve the material's $\mu_{\rm w}$. Band structures previously calculated for YbEuCdSb₂ indicate the presence of three bands within ~0.25 eV of the Fermi level. This idea is supported by Figure S7, which shows that samples, x=0.1, 0.2, 0.4, and 0.5, experience an increase in DOS near 400 K when the fermi Dirac distribution is broader. Calculations of the disordered structures would be necessary to confirm band convergence. The highest $\mu_{\rm w}$ is observed for x=0.3, which suggests that bonding is optimized in this composition. Interestingly, the same composition exhibits a drop in Yb1–Yb1 distances discussed above, which are thought to play an important role in the stability of this compound.

Given the high weighted mobility and expected band convergence in x = 0.3, it is surprising that the lowest Seebeck coefficient is reported for this sample. Further insight into this trend can be gained from examination of changes in the reduced Fermi level (η) , an indicator of the doping level calculated from Seebeck coefficients, 43 across the series. From Figure 11, it is apparent that x = 0.3 is the most heavily doped

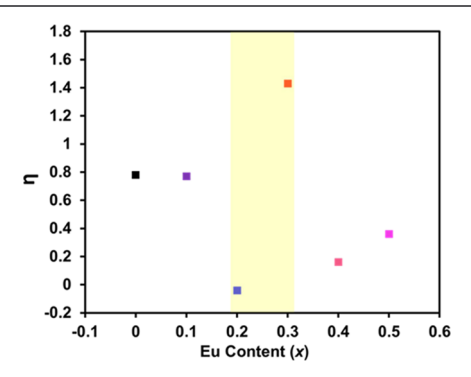


Figure 11. Reduced chemical potential for $Yb_{2-x}Eu_xCdSb_2$ at 525 K. The yellow box highlights compositions x = 0.2 and x = 0.3, which have the lowest and highest chemical potential.

at 525 K, which results in the lowest Seebeck coefficients and resistivity, despite having the highest weighted mobility. The reverse is true for x=0.2, which has the lowest carrier concentration and highest Seebeck coefficients despite having the lowest $\mu_{\rm w}$. The fluctuations in carrier concentration across the series make direct comparison of changes in thermoelectric properties difficult and highlight the usefulness of a carrier concentration independent factor such as $\mu_{\rm w}$ to help separate contributions from carrier concentration and changes in band structure. The changing carrier concentration also underscores the importance of understanding and controlling native defects to optimize thermoelectric performance.

The origin of the difference in carrier concentration can be understood by returning to cation and Sb vacancies. As described above, cation vacancies are expected to be the dominant defect in this system, so the sample with the largest number of cation vacancies is expected to have the highest carrier concentration, while the sample with the lowest carrier concentration would be expected to have nearly fully occupied cation sites. Figure 6c shows that the lowest Yb1 occupancy is observed for x = 0.3 at 0.93, which is consistent with the highest carrier concentration. However, x = 0.2 exhibits the second-lowest Yb1 occupancy at 0.94 but has the lowest carrier concentration. The discrepancy between the cation deficiency

and carrier concentration can be explained by the presence of a large amount of killer Sb defects in x = 0.2 compared to x = 0.20.3, with Sb2 site occupancies of 0.91 and 0.95, respectively (Figure 6c). One possible explanation for this difference is a change in orbital overlap that leads to differing COHP curves between samples. Previously calculated COHP curves show that the top of the valence band is composed of Yb1-Yb1 bonding states that stabilize the structure, along with Cd-Sb antibonding states just below the Yb1-Yb1 states. 19 The shorter Yb1-Yb1 distance in x = 0.3 increases the orbital overlap, increasing the Yb1-Yb1 bonding interaction just below the Fermi level, while the longer Yb1–Yb1 distance in x = 0.2 reduces orbital overlap and decreases the Yb1-Yb1 bonding interaction, pinning the Fermi level to a higher energy to avoid destabilizing the structure by emptying the Yb1-Yb1 bonding states and leaving the Cd-Sb antibonding states fully populated. For x = 0.3, stronger Yb1-Yb1 bonding character allows the Fermi level to be pushed deeper into the valence band before Sb defects begin compensating. COHP calculations for both compositions are necessary to confirm this explanation.

3.3. Thermal Properties. Total thermal conductivity (κ_{tot}) , shown in Figure 12a, is very low for such a simple structure and is higher for Eu-containing samples than the parent compound, consistent with previous reports. 11 Calculations on this system have confirmed the presence of lowfrequency optical phonon branches that can couple to acoustic branches and result in a large number of 3-phonon scattering channels which lower lattice thermal conductivity. Yb_{2-x}Eu_xCdSb₂ has also been compared to SnSe due to its anomalously low thermal conductivity, which for SnSe has been attributed to strong anharmonicity arising from soft, anisotropic bonding in its zig-zag structure⁴⁵⁻⁴⁸ and, more recently, an unstable electronic structure and electron-phonon coupling resulting in polaron formation. 47,49 These factors could play a role in this system, as well, given the similar morphology of the zig-zag layers, distorted bonding, and presence of localized Sb 5s² lone pairs. Recent work on structures with zig-zag layers, such as Cu₃SbSe₃, SnSe, and Cu₁₂Sb₃Se₁₃, has shown that the repulsion between the Sb/Sn lone pair and bonding pairs in the covalent chains contributes to anharmonicity and soften phonon modes. 48 Lattice thermal conductivity for Yb2-xEuxCdSb2 is lower for compositions that have higher Sb2 site occupancies (x = 0, 0.1, and 0.3), suggesting that the lone pair localized on the Sb2 site plays a role in phonon scattering.

The electronic portion of the thermal conductivity ($\kappa_{\rm e}$), shown in Figure 12b, was calculated using the Wiedemann–Franz relation ($\kappa_{\rm e}=LT/\rho$), where L is the Lorenz number and was estimated using the Seebeck coefficient. $\kappa_{\rm e}$ trends as expected based on electrical resistivity, with the least resistive $\kappa_{\rm e}=0.3$ composition exhibiting the largest $\kappa_{\rm e}=0.3$ and highest contribution to thermal conductivity, $\kappa_{\rm L}$, estimated by subtracting $\kappa_{\rm e}$ from $\kappa_{\rm tov}$ is the lowest for $\kappa_{\rm e}=0.3$ and highest for $\kappa_{\rm e}=0.3$ at 525 K (Figure 12c). The extremely low $\kappa_{\rm L}$ for $\kappa_{\rm e}=0.3$ is likely due to local disorder in this highly defected composition discussed above, as well as the large unit cell volume.

3.4. Thermoelectric Quality Factor (B). The high weighted mobility, μ_w , and low lattice thermal conductivity in the highly defected x = 0.3 composition of $Yb_{2-x}Eu_xCdSb_2$ make it a promising candidate for further optimization. To assess its potential, the thermoelectric quality factor (B) was

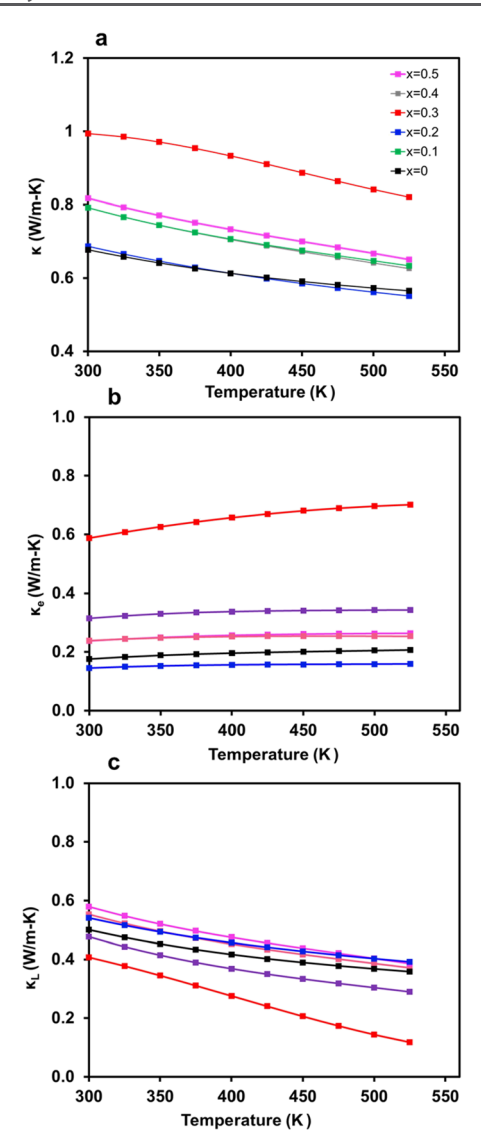


Figure 12. (a) Total thermal conductivity, (b) electronic component of thermal conductivity, (c) lattice component of thermal conductivity for Yb_{2-x}Eu_xCdSb₂.

employed. B uses $\mu_{\rm w}$ and $\kappa_{\rm L}$ to predict the highest possible zT for a given material at a given temperature if the carrier concentration is optimized. The highest value was observed at 525 K for x=0.3, $B\approx 1.5$ (Table 3, Figure 13), which predicts a maximum zT>2 if the carrier concentration is sufficiently reduced. Thermoelectric efficiency predictions based on B assume isotropic bands in which effective mass does not change when the Fermi level moves. Yb_{2-x}Eu_xCdSb₂ is a layered phase with anisotropic bonding so B predictions may

Table 3. Thermoelectric Quality Factor (B) for Yb_{2-x}Eu_xCdSb₂ at 525 K

x	В
0	0.22
0.1	0.42
0.2	0.27
0.3	1.45
0.4	0.39
0.5	0.31

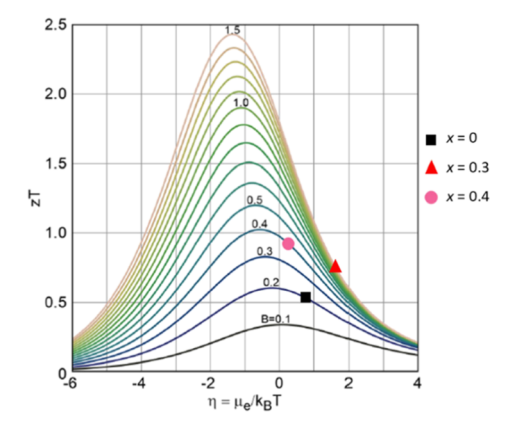


Figure 13. Quality factor (*B*) plotted as a function of reduced chemical potential (η) and zT. *B* values at 525 K for select Yb_{2-x}Eu_xCdSb₂ samples are shown color-coded as filled circles. The zT vs η showing *B* plot is reprinted from reference 51 with permission of AIP Publishing.

not be attainable, as reducing the carrier concentration in Yb_{2-x}Eu_xCdSb₂ may also alter the transport properties. However, given the exceedingly high *B* value of the heavily defected Yb_{1.7}Eu_{0.3}CdSb₂, further optimization of this composition is of interest. Lu³⁺ would be a good candidate to reduce carrier concentration and would most likely occupy the Yb2 site; given its smaller size and higher electronegativity, ¹⁹ it is not expected to alter the valence band edge.

4. CONCLUSIONS

Thermoelectric properties in the Yb_{2-x}Eu_xCdSb₂ solid solution are heavily impacted by disorder and defects, and defect structure needs to be considered alongside composition to optimize efficiency. The best performing composition was found to be x = 0.4, with $zT \approx 0.9$ at 525 K, making this compound the highest efficiency p-type Zintl phase at low temperatures (Figure 14).⁵ If defects can be controlled through the synthetic method and the carrier concentration can be reduced, the thermoelectric quality factor predicts that Yb_{2-x}Eu_xCdSb₂ could achieve a zT of ~2.5 at 525 K. This

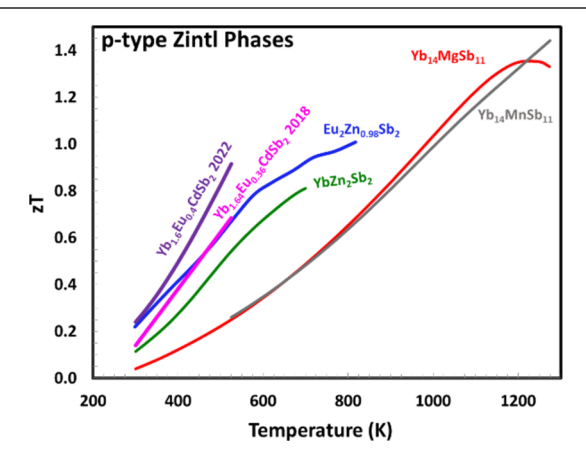


Figure 14. zT as a function of temperature for leading p-type Zintl phases, $Yb_{1.64}Eu_{0.36}CdSb_2$, 11 $Eu_2Zn_{0.98}Sb_2$, 9 $YbZn_2Sb_2$, 12 $Yb_{14}MgSb_{11}$, 52 and $Yb_{14}MnSb_{11}$, 53 $Yb_{1.6}Eu_{0.4}CdSb_2$ from this work (purple) gives a higher zT across the low-temperature range (300–525 K) than any other material shown. A plot of the zTs for $Yb_{2.x}Eu_xCdSb_2$ from from 300–525 K is provided as Figure S8.

work highlights the importance of understanding defects from a structure and bonding point of view to optimize thermoelectric properties. Employing COHP curves together with PDF analysis of local structure enables thermoelectric properties to be tuned using chemical intuition via substitution on relevant crystallographic sites while providing a detailed understanding of defect chemistry. These concepts can be applied to other promising thermoelectric materials to help understand and control electronic properties.

ASSOCIATED CONTENT

Solution Supporting Information

The Supporting Information is available free of charge at https://pubs.acs.org/doi/10.1021/acs.chemmater.2c02402.

EDS spectrum, SEM micrographs and EDS maps, Rietveld refinements and statistics, PDF refinements, Seebeck coefficients with single parabolic band contours, and *zT*'s for all polycrystalline samples (PDF)

Data of $Yb_{2-x}Eu_xCdSb_2x = 0.22$ (CIF)

Data of $Yb_{2-x}Eu_xCdSb_2x = 0.29$ (CIF)

Data of $Yb_{2-x}Eu_xCdSb_2x = 0.42$ (CIF)

AUTHOR INFORMATION

Corresponding Author

Susan M. Kauzlarich – Chemistry Department, University of California, Davis, California 95616, United States;

orcid.org/0000-0002-3627-237X; Email: smkauzlarich@ucdavis.edu

Authors

Ashlee K. Hauble — Chemistry Department, University of California, Davis, California 95616, United States;
orcid.org/0000-0002-2794-9916

Caitlin M. Crawford – Department of Physics, Colorado School of Mines, Golden, Colorado 80401, United States

Jesse M. Adamczyk – Department of Physics, Colorado School of Mines, Golden, Colorado 80401, United States

Maxwell Wood – Thermal Energy Conversion Research and Advancement Group, Jet Propulsion Laboratory, California Institute of Technology, Pasadena, California 91109-8099, United States

James C. Fettinger – Department of Physics, Colorado School of Mines, Golden, Colorado 80401, United States;
orcid.org/0000-0002-6428-4909

Eric S. Toberer – Department of Physics, Colorado School of Mines, Golden, Colorado 80401, United States

Complete contact information is available at: https://pubs.acs.org/10.1021/acs.chemmater.2c02402

Notes

The authors declare no competing financial interest.

■ ACKNOWLEDGMENTS

This work was supported by NSF DMR-2001156 and NSF DMR-1555340. This research used resources of the Advanced Photon Source; a U.S. Department of Energy (DOE) Office of Science User Facility operated for the DOE Office of Science by Argonne National Laboratory under Contract No. DE-AC02-06CH11357. The mail-in program at Beamline 11-ID-B (and/or 17-BM, 11-BM) contributed to the data. We thank the National Science Foundation (Grant CHE-1531193 and CHE-0840444) for the Dual Source X-ray diffractometers.

Funding for this work was also received from the University of California, Davis Dean's Distinguished Graduate Student Fellowship. This research used the Advanced Materials Characterization and Testing laboratory (AMCaT) for SEM/EDS data. We thank Dr. Kasey P. Devlin for useful discussion and Jennifer Liem for preliminary experimental work.

REFERENCES

- (1) Fleurial, J. P. Thermoelectric Power Generation Materials: Technology and Application Opportunities. *J. Miner. Met. Mater. Soc.* **2009**, *61*, 79–85.
- (2) Fleurial, J.-P.; Borshchevsky, A.; Caillat, T.; Ewell, R.New Materials and Devices for Thermoelectric Applications. In Proceedings of the Intersociety Energy Conversion Engineering Conference; IEEE: Honolulu, HI, USA, 1997; pp 1080–1085.
- (3) Liu, K. F.; Xia, S. Q. Recent Progresses on Thermoelectric Zintl Phases: Structures, Materials and Optimization. *J. Solid State Chem.* **2019**, 270, 252–264.
- (4) Lee, K. H.; Kim, J. Y.; Choi, S. M. Recent Progress in Bi-Te-Based Thermoelectric Materials. *J. Korean Ceram. Soc.* **2015**, *52*, 1–8.
- (5) Shuai, J.; Mao, J.; Song, S.; Zhang, Q.; Chen, G.; Ren, Z. Recent Progress and Future Challenges on Thermoelectric Zintl Materials. *Mater. Today Phys.* **2017**, *1*, 74–95.
- (6) Snyder, G. J.; Toberer, E. S. Complex Thermoelectric Materials. *Nat. Mater.* **2008**, *7*, 105–114.
- (7) Perez, C. J.; Wood, M.; Ricci, F.; Yu, G.; Vo, T.; Bux, S. K.; Hautier, G.; Rignanese, G.-M.; Snyder, G. J.; Kauzlarich, S. M. Discovery of Multivalley Fermi Surface Responsible for the High Thermoelectric Performance in Yb₁₄MnSb₁₁ and Yb₁₄MgSb₁₁. *Sci. Adv.* **2021**, *7*, No. eabe9439.
- (8) Yao, H.; Chen, C.; Xue, W.; Bai, F.; Cao, F.; Lan, Y.; Liu, X.; Wang, Y.; Singh, D. J.; Lin, X.; Zhang, Q. Vacancy Ordering Induced Topological Electronic Transition in Bulk Eu₂ZnSb₂. *Sci. Adv.* **2021**, 7, 1–7.
- (9) Chen, C.; Xue, W.; Li, S.; Zhang, Z.; Li, X.; Wang, X.; Liu, Y.; Sui, J.; Liu, X.; Cao, F.; Ren, Z.; Chu, C.-W.; Wang, Y.; Zhang, Q. Zintl-Phase Eu₂ZnSb₂: A Promising Thermoelectric Material with Ultralow Thermal Conductivity. *Proc. Natl. Acad. Sci. U. S. A.* **2019**, *116*, 2831–2836.
- (10) Chanakian, S.; Uhl, D.; Neff, D.; Drymiotis, F.; Park, J.; Petkov, V.; Zevalkink, A.; Bux, S. Exceptionally High Electronic Mobility in Defect-Rich Eu₂ZnSb_{2-x}Bi_x Alloys. *J. Mater. Chem. A* **2020**, *8*, 6004–6012.
- (11) Cooley, J. A.; Promkhan, P.; Gangopadhyay, S.; Donadio, D.; Pickett, W. E.; Ortiz, B. R.; Toberer, E. S.; Kauzlarich, S. M. High Seebeck Coefficient and Unusually Low Thermal Conductivity Near Ambient Temperatures in Layered Compound Yb_{2-x}Eu_xCdSb₂. *Chem. Mater.* **2018**, *30*, 484–493.
- (12) Zevalkink, A.; Zeier, W. G.; Cheng, E.; Snyder, J.; Fleurial, J. P.; Bux, S. Nonstoichiometry in the Zintl Phase $Yb_{1-\delta}Zn_2Sb_2$ as a Route to Thermoelectric Optimization. *Chem. Mater.* **2014**, *26*, 5710–5717.
- (13) Lin, J.; Li, X.; Qiao, G.; Wang, Z.; Carrete, J.; Ren, Y.; Ma, L.; Fei, Y.; Yang, B.; Lei, L.; Li, J. Unexpected High-Temperature Stability of β -Zn₄Sb₃ Opens the Door to Enhanced Thermoelectric Performance. *J. Am. Chem. Soc.* **2014**, *136*, 1497–1504.
- (14) Caillat, T.; Fleurial, J. P.; Borshchevsky, A. Preparation and Thermoelectric Properties of Semiconducting Zn₄Sb₃. *J. Phys. Chem. Solids* **1997**, *58*, 1119–1125.
- (15) Toberer, E. S.; Rauwel, P.; Gariel, S.; Taftø, J.; Snyder, G. J. Composition and the Thermoelectric Performance of β -Zn₄Sb₃. *J. Mater. Chem.* **2010**, 20, 9877–9885.
- (16) Perumal, S.; Roychowdhury, S.; Biswas, K. High Performance Thermoelectric Materials and Devices Based on GeTe. *J. Mater. Chem. C* **2016**, *4*, 7520.
- (17) Ovchinnikov, A.; Bobev, S. Zintl Phases with Group 15 Elements and the Transition Metals: A Brief Overview of Pnictides with Diverse and Complex Structures. *J. Solid State Chem.* **2019**, 270, 346–359.

- (18) Xia, S. Q.; Bobev, S. Cation-Anion Interactions as Structure Directing Factors: Structure and Bonding of Ca₂CdSb₂ and Yb₂CdSb₃. *J. Am. Chem. Soc.* **2007**, *129*, 4049–4057.
- (19) Kim, K.; Lee, J.; Shin, S.; Jo, H.; Moon, D.; Ok, K. M.; You, T.-S. Chemical Driving Force for Phase-Transition in the $Ca_{2-x}RE_xCdSb_2$ (RE = Yb, Eu; $011(1) \le x \le 1.36(2)$) System. Cryst. Growth Des. **2020**, 20, 746–754.
- (20) Devlin, K. P.; Chen, S.; Donadio, D.; Kauzlarich, S. M. Solid Solution Yb_{2-x}Ca_xCdSb₂: Structure, Thermoelectric Properties, and Quality Factor. *Inorg. Chem.* **2021**, *60*, 13596–13606.
- (21) Pomrehn, G. S.; Zevalkink, A.; Zeier, W. G.; Van De Walle, A.; Snyder, G. J. Defect-Controlled Electronic Properties in AZn₂Sb₂ Zintl Phases. *Angew. Chem., Int. Ed.* **2014**, *53*, 3422–3426.
- (22) Qu, J.; Balvanz, A.; Baranets, S.; Bobev, S.; Gorai, P. Computational Design of Thermoelectric Alloys through Optimization of Transport and Dopability. *Mater. Horizons* **2022**, *9*, 720–730.
- (23) Ogunbunmi, M. O.; Baranets, S.; Bobev, S. Structural Complexity and Tuned Thermoelectric Properties of a Polymorph of the Zintl Phase Ca₂CdSb₂ with a Non-Centrosymmetric Monoclinic Structure. *Inorg. Chem.* **2022**, *61*, 10888–10897.
- (24) Zhang, J.; Song, L.; Iversen, B. B. Insights into the Design of Thermoelectric Mg₃Sb₂ and Its Analogs by Combining Theory and Experiment. *npj Comput. Mater.* **2019**, *S*, 1–17.
- (25) Zhang, J.; Song, L.; Sist, M.; Tolborg, K.; Iversen, B. B. Chemical Bonding Origin of the Unexpected Isotropic Physical Properties in Thermoelectric Mg₃Sb₂ and Related Materials. *Nat. Commun.* **2018**, *9*, 4716.
- (26) Cao, Q.-G.; Zhang, H.; Tang, M.-B.; Chen, H. H.; Yang, X. X.; Grin, Y.; Zhao, J. T. Zintl Phase with Tunable Thermoelectric Properties Induced by Cation Substitution. *J. Appl. Phys.* **2010**, *107*, 53714.
- (27) Alemneh Wubieneh, T.; Wei, P.; Yeh, C.; Chen, S.; Chen, Y. Thermoelectric Properties of Zintl Phase Compounds of $Ca_{1-x}Eu_xZn_2Sb_2$ (0 \leq x \leq 1). J. Electron. Mater. **2016**, 45, 1942–1946.
- (28) Zhang, H.; Fang, L.; Tang, M.-B.; Man, Z. Y.; Chen, H. H.; Yang, X. X.; Baitinger, M.; Grin, Y.; Zhao, J.-T. Thermoelectric Properties of Yb_xEu_{1-x}Cd₂Sb₂. *J. Chem. Phys.* **2010**, *133*, 194701.
- (29) Devlin, K. P.; Chen, S.; Donadio, D.; Kauzlarich, S. M. Solid Solution Yb₂Ca_xCdSb₂: Structure, Thermoelectric Properties, and Quality Factor. *Inorg. Chem.* **2021**, *60*, 13596–13606.
- (30) Saparov, B.; Saito, M.; Bobev, S. Syntheses, and Crystal and Electronic Structures of the New Zintl Phases Na_2ACdSb_2 and K_2ACdSb_2 (A = Ca, Sr, Ba, Eu, Yb): Structural Relationship with Yb_2CdSb_2 and the Solid Solutions $Sr_{2-x}A_xCdSb_2$, $Ba_{2-x}A_xCdSb_2$ and $Eu_{2-x}Yb_xCdSb_2$. *J. Solid State Chem.* **2011**, *184*, 432–440.
- (31) Canfield, P. C.; Kong, T.; Kaluarachchi, U. S.; Jo, N. H. Use of Frit-Disc Crucibles for Routine and Exploratory Solution Growth of Single Crystalline Samples. *Philos. Mag.* **2016**, *96*, 84–92.
- (32) Bruker AXS; TOPAS Version 5; 2014.
- (33) Toby, B. H.; Von Dreele, R. B. GSAS-II: The Genesis of a Modern Open-Source All Purpose Crystallography Software Package. *J. Appl. Crystallogr.* **2013**, *46*, 544–549.
- (34) Zhou, X.-J.; Tao, J.-Z.; Guo, H.; Lin, H. Atomic Pair Distribution Function Method Development at the Shanghai Synchrotron Radiation Facility. *Chin. Phys. B* **2017**, *26*, No. 076101.
- (35) Iwanaga, S.; Toberer, E. S.; Lalonde, A.; Snyder, G. J. A High Temperature Apparatus for Measurement of the Seebeck Coefficient. *Rev. Sci. Instrum.* **2011**, *82*, No. 063905.
- (36) Borup, K. A.; Toberer, E. S.; Zoltan, L. D.; Nakatsukasa, G.; Errico, M.; Fleurial, J.-P.; Iversen, B. B.; Snyder, G. J. Measurement of the Electrical Resistivity and Hall Coefficient at High Temperatures. *Rev. Sci. Instrum.* **2012**, *83*, 123902.
- (37) Borup, K. A.; de Boor, J.; Wang, H.; Drymiotis, F.; Gascoin, F.; Shi, X.; Chen, L.; Fedorov, M. I.; Eckhard, M.; Iversen, B. B.; Snyder, J. G. Measuring Thermoelectric Transport Properties of Materials. *Energy Environ. Sci.* **2015**, *8*, 423–435.
- (38) Ovchinnikov, A.; Darone, G. M.; Saparov, B.; Bobev, S. Exploratory Work in the Quaternary System of Ca-Eu-Cd-Sb:

Synthesis, Crystal, and Electronic Structures of New Zintl Solid Solutions. *Materials* **2018**, *11*, 1–13.

- (39) Lee, J.; Ahn, K.; Kim, K.; Jo, H.; Yoon, J. S.; Moon, D.; Shin, W. H.; Kang, M. O.; You, T.-S. Effect of Rare-Earth Metals Substitution for Ca on the Crystal Structure and Thermoelectric Properties of the Ca_{10-x}RE_xSb_{10-y} System. *Cryst. Growth Des.* **2019**, *19*, 3498–3508.
- (40) Gorai, P.; Goyal, A.; Toberer, E. S.; Stevanović, V. A Simple Chemical Guide for Finding Novel N-Type Dopable Zintl Pnictide Thermoelectric Materials. *J. Mater. Chem. A* **2019**, *7*, 19385–19395.
- (41) Balvanz, A.; Qu, J.; Baranets, S.; Ertekin, E.; Gorai, P.; Bobev, S. New n-Type Zintl Phases for Thermoelectrics: Discovery, Structural Characterization, and Band Engineering of the Compounds A_2CdP_2 (A = Sr, Ba, Eu). *Chem. Mater.* **2020**, *32*, 10697–10707.
- (42) Kazem, N.; Zaikina, J. V.; Ohno, S.; Snyder, G. J.; Kauzlarich, S. M. Coinage-Metal-Stuffed Eu₉Cd₄Sb₉: Metallic Compounds with Anomalous Low Thermal Conductivities. *Chem. Mater.* **2015**, 27, 7508–7519.
- (43) Snyder, G. J.; Snyder, A. H.; Wood, M.; Gurunathan, R.; Snyder, B. H.; Niu, C. Weighted Mobility. *Adv. Mater.* **2020**, 32, No. 2001537.
- (44) May, A. F.; Snyder, G. J.Introduction to Modeling Thermoelectric Transport at High Temperatures. In *Materials, Preparation, and Characterization in Thermoelectrics*; CRC Press, 2017; p 11.
- (45) Liu, G.; Zhou, J.; Wang, H. Anisotropic Thermal Expansion of SnSe from First-Principles Calculations Based on Grü Neisen's Theory. *Phys. Chem. Chem. Phys.* **2017**, *19*, 15187.
- (46) Liu, F.; Parajuli, P.; Rao, R.; Wei, P. C.; Karunarathne, A.; Bhattacharya, S.; Podila, R.; He, J.; Maruyama, B.; Priyadarshan, G.; Gladden, J. R.; Chen, Y. Y.; Rao, A. M. Phonon Anharmonicity in Single-Crystalline SnSe. *Phys. Rev. B* **2018**, *98*, No. 224309.
- (47) Li, C. W.; Hong, J.; May, A. F.; Bansal, D.; Chi, S.; Hong, T.; Ehlers, G.; Delaire, O. Orbitally Driven Giant Phonon Anharmonicity in SnSe. *Nat. Phys.* **2015**, *11*, 1063–1069.
- (48) Zhang, Y. First-Principles Debye—Callaway Approach to Lattice Thermal Conductivity. J. Mater. 2016, 2, 237–247.
- (49) René De Cotret, L. P.; Otto, M. R.; Pöhls, J.-H.; Luo, Z.; Kanatzidis, M. G.; Siwick, B. J. Direct Visualization of Polaron Formation in the Thermoelectric SnSe. *Proc. Natl. Acad. Sci. U. S. A.* **2022**, *119*, No. e2113967119.
- (50) Kim, H. S.; Gibbs, Z. M.; Tang, Y.; Wang, H.; Snyder, G. J. Characterization of Lorenz Number with Seebeck Coefficient Measurement. *APL Mater.* **2015**, *3*, No. 041506.
- (51) Zevalkink, A.; Smiadak, D. M.; Blackburn, J. L.; Ferguson, A. J.; Chabinyc, M. L.; Delaire, O.; Wang, J.; Kovnir, K.; Martin, J.; Schelhas, L. T.; Sparks, T. D.; Kang, S. D.; Dylla, M. T.; Snyder, G. J.; Ortiz, B. R.; Toberer, E. S. A Practical Field Guide to Thermoelectrics: Fundamentals, Synthesis, and Characterization. *Appl. Phys. Rev.* 2018, 5, No. 021303.
- (52) Perez, C. J.; Chen, Z.; Beeson, W. B.; Chanakian, S.; Liu, K.; Bux, S. K.; Kauzlarich, S. M. Chemical Route to Yb₁₄MgSb₁₁ Composites with Nanosized Iron Inclusions for the Reduction of Thermal Conductivity. *ACS Appl. Energy Mater.* **2021**, *4*, 3748–3756.
- (53) Li, B.; Firdosy, S.; Paik, J. A.; Huang, C. K.; Cheng, B.; Gogna, P.; Nakatsukasa, G.; Caillat, T.; Fleurial, J. P.; Ravi, V.; Nesmith, B.; Ewell, R.; Brandon, E. J. Development of New High Temperature Power Generating Couples for the Advanced Thermoelectric Converter (ATEC). In 8th Annual International Energy Conversion Engineering Conference; 2010; Vol. 2010, pp 1–7.